



OPEN Characterization of human trabecular bone across multiple length scales using a correlative approach combining X-ray tomography with LaserFIB and plasma FIB-SEM

Tengteng Tang^{1,2}✉, Travis Casagrande³, Pardis Mohammadpour³, William Landis⁴, Brent Liewers⁵ & Kathryn Grandfield¹

Three-dimensional correlative multimodal and multiscale imaging is an emerging method for investigating the complex hierarchical structure of biological materials such as bone. This approach synthesizes images acquired across multiple length scales, for the same region of interest, to provide a comprehensive view of the material structure of a sample. Here, we develop a workflow for the structural analysis of human trabecular bone using a femtosecond laser to produce a precise grid to facilitate correlation between imaging modalities and identification of structures of interest, in this case, a single trabecula within a volume of trabecular bone. Through such image registration, high resolution X-ray microscopy imaging revealed fine architectural details, including the cement sheath and bone cell lacunae of the selected bone trabecula. The selected bone volume was exposed with a combination of manual polishing and site-specific femtosecond laser ablation and then examined with plasma focused ion beam-scanning electron microscopy. This reliable and versatile correlation approach has the potential to be applied to a variety of biological tissues and traditional engineered materials. The proposed workflow has the enhanced capability for generating highly resolved and broadly contextualized structural data for a better understanding of the architectural features of a material spanning its macroscopic to nanoscopic levels.

Structural hierarchy describes the tiered organization of distinct structural features of a material at multiple length or size scales and is an extremely important means for characterizing many synthetic and engineering materials, as well as biological materials such as bone. Understanding the hierarchical organization of both engineered and biological materials is critical to determining their fundamental attributes, including their mechanical properties, failure behavior, chemical or biochemical reactivity, and metabolic availability among other basic features. Bone tissue is of particular interest for investigation given that it adapts to a variety of factors such as exercise and additional forms of physical activity, diet, aging, disease, and environmental conditions, all of which provide a range of normal and pathological structures that lead to knowledge of its underlying structure-property relationships. The three-dimensional (3D) arrangement of bone structural elements at each hierarchical level, from gross anatomical to micro-, nano-, and subnanometer dimensions, governs bone behavior, including its strength, toughness, and other mechanical properties, such as elastic modulus, hardness, viscoelasticity, fatigue, and damage tolerance^{1,2}. This structural interplay across different length scales influences various functions of bone, which not only provide mechanical support for the body and protection of internal organs but also facilitate adaptation to the environment and enable other critical biological functions^{3,4}.

¹Department of Materials Science and Engineering, McMaster University, Hamilton, Canada. ²Center for Applied Biomechanics, Department of Mechanical and Aerospace Engineering, School of Engineering and Applied Science, University of Virginia, Charlottesville, USA. ³Canadian Centre for Electron Microscopy, McMaster University, Hamilton, Canada. ⁴Department of Preventive and Restorative Dental Sciences, University of California at San Francisco, San Francisco, USA. ⁵Bharti School of Engineering and Computer Science, Laurentian University, Sudbury, Canada. ✉email: bav7wh@virginia.edu

Moreover, structural hierarchy information, correlated in 3D across different length or size scales, can provide novel insights for designing better performing engineered constructs.

Investigating the 3D hierarchical structure of biological materials is non-trivial. The vertebrate skeleton, for example, has as many as 12 levels of hierarchy, ranging from its mineralized collagen fibrils at a nanometer scale, to osteons at micrometer scale units, and then to cortical and trabecular bone tissue at the macroscopic scale^{1,4,5}. Although there are many techniques available to study the 3D structure of bone at these various length scales and volumes, none is capable of capturing bone architecture across all its relevant measures. Furthermore, each method has its own distinct advantages and shortcomings^{6–9} with many involving a compromise between the imaging resolution and the volume that can be probed. For X-ray based tools, micro-computed tomography (micro-CT) has the benefit of capturing micrometer-scaled features, such as osteons and bone cells (osteoblasts/osteocytes), but it lacks the resolution to yield ultrastructural details. Recent advances in synchrotron-radiation nanotomography (SR nanoCT) allow for sub-25 nm voxel size visualization of small samples under transmission X-ray microscopy, and techniques such as ptychography achieve even higher resolution¹⁰. However, SR nanoCT, in particular ptychographic tomography, presents limitations such as radiation damage to the sample¹¹ and a limited field of view¹². Electron-based 3D volume analysis, such as focused ion beam-scanning electron microscope (FIB-SEM) tomography, has emerged as a critical approach for studying mineralized tissues at the ultrastructural level. FIB-SEM has the capability to produce nanoscale resolution images over tens of micrometers of tissue volume. Recent advances with this technique have enabled precise milling of biomineralized tissues for TEM lamella preparation^{13–15} and have led to detailed examination and documentation of bone features such as mineral ellipsoids^{16,17}, collagen banding^{18,19}, and nanochannel structures^{20,21} across multiple layers of bone lamellae. Similarly, transmission electron microscopy (TEM) tomography probes at even higher resolution to distinguish components such as individual mineral particles and collagen fibrils, but it is restricted to extremely thin (~ 100 nm) material sections of very small volume²².

Combining several of the imaging modalities mentioned above can help construct a more complete 3D picture of structural features over length scales bridging tissue (macroscopic) to nanometer levels. For example, it has been shown that the orientation of collagen fibrils and their associated mineral platelets in human trabecular bone at the nanoscale is associated with the surface curvature at the microscale^{23,24}. However, many previous studies have commonly used various techniques applied in parallel to different samples, and the resulting data have been brought together through a qualitative or a statistical approach. This means of analysis, however, may lead to misrepresentation and/or misinterpretation of sample structural features²⁵. Recent advances in the instrumentation for 3D X-ray microscopy (XRM), FIB processing, and FIB-SEM volume imaging have the potential to address these difficulties through correlative tomography. Compared to previous generations of micro-CT imaging, the latest XRM combines geometric magnification and scintillator-coupled optics for different magnifications, allowing for higher spatial resolution at longer working distances²⁶. Further, it is now possible to use XRM for identifying, isolating, and probing the specific inner structure of a sample to generate higher resolution scans^{27,28}. Alongside this development, advances in serial sectioning using Ga or Xe FIB milling have broadened the application by expanding the length scales of 3D acquisition from tens to hundreds of micrometers²⁹. Additionally, femtosecond (fs) lasers have become increasingly valuable for processing large sample volumes (millimeters). The fs laser is an ultra-short pulse laser with pulse lengths typically ranging from several dozen to a few hundred femtoseconds^{30,31}, a feature which enables rapid material removal to reveal regions of interest (ROIs) deeply buried within the sample. More importantly, the heat-affected zone is minimized largely because of athermal material ablation³¹, thus providing safe ablation with close proximity to the targeted regions. While previous studies have utilized fs lasers alongside imaging modalities such as SEM, optical microscopy or XRM to target specific ROIs for sample preparation^{30,32,33}, the complex hierarchical structures of materials, such as biological tissues and semiconductor devices, demand targeting capabilities that extend beyond the surface to subsurface regions. Further, these beam-sensitive materials require site-specific precision on a micrometer scale for effective sample processing and subsequent FIB-SEM imaging and analysis.

In this study, we establish a novel analytical workflow capable of examining structural hierarchy across multiple length scales utilizing correlative 3D X-ray and electron imaging applied to investigate aspects of human trabecular bone structure (Fig. 1). This workflow involves the sequential use of several instruments and methods, beginning with the creation of a customized grid on the specimen surface using an fs laser (a Zeiss LaserFIB, see Materials and methods), followed by low and progressively higher resolution XRM scans at the micrometer scale of selected subsurface ROIs of the bone sample. Subsequently, an XRM tomography volume obtained is linked to live SEM imaging of the sample surface to guide site-specific LaserFIB preparation of the selected ROI for plasma FIB-SEM (PFIB-SEM) tomography. The trabecular bone cross sections exposed by laser ablation are then finally processed by PFIB-SEM tomography acquisition at the nanometer scale. Each of these sequential steps will be described in more detail below as they relate to the investigation and analysis of the human trabecular bone sample. The workflow demonstrates the value of this approach for studying biological and engineering materials across multiple length scales.

Materials and methods

Specimen preparation

A human trabecular bone sample (~10×5×5 mm³) was obtained for this study from the region close to the lesser trochanter of an adult donor without any known bone disease. The sample was acquired from the donor with informed consent and all methods and experimental protocols were approved and carried out in accordance with relevant guidelines and regulations from the institutional ethics board (HiREB No. T-2289, McMaster University, ON, Canada).

The bone tissue was frozen at – 20 °C until specimen preparation. After thawing, the tissue was fixed in 4% paraformaldehyde (Electron Microscopy Sciences, Hatfield, PA, USA) in phosphate-buffered saline solution

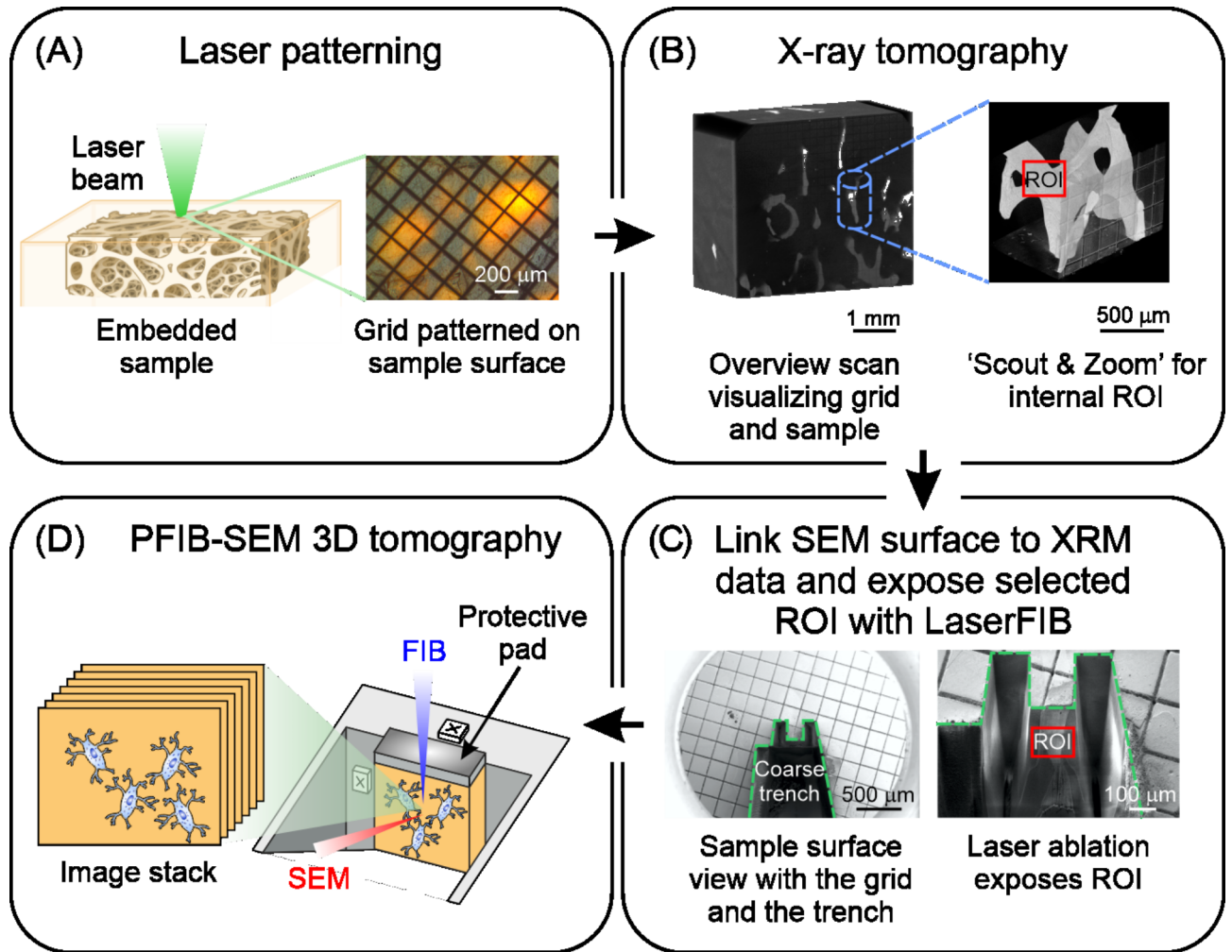


Fig. 1. Correlative tomography workflow applied to studying ultrastructural features in human trabecular bone. (A) A schematic diagram of an embedded human trabecular bone sample and an optical image showing the coordinate grid created by LaserFIB (green beam). (B) Progressively higher resolution X-ray tomography scans defining an internal region of interest (ROI) with respect to the surface grid. (C) SEM images of a sample with its ROI exposed by LaserFIB processing. The surface grid was used to link the XRM data to the sample position in live SEM imaging to target the chosen internal ROI, which was subsequently revealed by LaserFIB processing. (D) A schematic diagram of the setup for PFIB-SEM serial sectioning and a stack of serial images obtained from the ROI by this process. A protective pad was deposited on the sample surface, which was oriented normal to the FIB (blue beam). Two fiducial marks were created next to the protective pad and the exposed cross section of the ROI, respectively. Following each FIB milling iteration, the SEM (red beam) captured images of the newly exposed ROI. This iterative process of FIB milling followed by SEM imaging was repeated to generate a stack of serial micrographs.

(PBS; Sigma-Aldrich, St. Louis, MO, USA) for 16 h and rinsed in 0.01 M PBS (Sigma-Aldrich) for 48 h. The bone sample was next dehydrated in a graded ethanol series (70%, 80%, 96%, 100%; 2 days for each step) before being embedded in Epon resin (Embed 812, Electron Microscopy Sciences). The embedded sample was then ground using sequentially finer carbide grinding papers to expose the transverse aspect of the bone (the aspect that is perpendicular to the long bone axis), which was subsequently polished with a diamond suspension of 3 µm followed by 1 µm particle size. While any aspect of the bone specimen was sufficient to allow the trabecular interior to be visible on the surface, the transverse aspect, parallel to the base of the embedding mold, was easiest to access and was selected for this reason.

Femtosecond laser creation of a coordinate grid

The embedded trabecular bone sample was mounted on a standard aluminum SEM stub and plasma sputter-coated with gold to provide a conductive surface for SEM imaging. The coordinate grid was created using a Zeiss Crossbeam 350 LaserFIB (Carl Zeiss Microscopy, Oberkochen, Germany), which is a FIB-SEM integrated with a femtosecond micro-machining laser system (TRUMPF SE + Co. KG, Ditzingen, Germany). The system utilized a wavelength of 515 nm, focused spot size < 15 µm, 350 fs pulse duration, maximum pulse energy of

10 μJ , maximum average power of 10 W, repetition rate ranging from 100 Hz to 1 MHz, 6 mm Z-focus range, $40 \times 40 \text{ mm}^2$ scan field, and selected operation in burst-mode (Fig. 1A). The laser processing occurred in an airlock, separate from the Crossbeam FIB-SEM chamber, so as to avoid contamination from laser ablation debris. Site-specific laser processing, with accuracy on the scale of a few micrometers, was enabled by SEM stage position registration of the specimen ROIs and also fiducial aperture locations on the laser specimen holder, followed by moving the laser specimen holder into the airlock and then laser scanning registration of the fiducial apertures³⁴. This process allowed the accurate positional placement of the SEM ROI images into the laser CAD software such that laser processing was precisely positioned over the specimen ROIs. The coordinate grid spanned an area of approximately $10 \text{ mm} \times 7 \text{ mm}$. The grid lines were $200 \mu\text{m}$ apart and $14 \mu\text{m}$ wide, and they extended approximately $10 \mu\text{m}$ into the resin surface. The major laser user parameters were 70% of maximum power, 10 mm/s velocity, 10 kHz pulse frequency, and one pass over the lines and characters, yielding an 80 s ablation time for the whole grid pattern.

X-ray microscopy (XRM)

The grid-patterned trabecular bone sample was scanned using a Zeiss Xradia 630 Versa X-ray microscope (XRM, Carl Zeiss Microscopy) for 3D tomography (Fig. 1B). The sample was attached to the end of a few cm-long pin using epoxy resin adhesive and mounted onto a Zeiss specimen holder for scanning. An overview scan generated reconstructed volumes with $\sim 6 \mu\text{m}$ isotropic voxels and was first performed at 40 kV, 3 W, 2401 projections over 360° of sample rotation, and 14 s exposure time per frame. A relatively longer exposure time was necessary for acquiring overview scans of the specimen at low (40 kV) voltage so that both individual bone trabeculae and the LaserFIB-patterned grid could be visualized. This dataset yielded information of ROIs in relation to the surface coordinate grid, which was essential for accurately targeting the ROIs with subsequent laser processing in site-specific preparation for further microscopy analysis such as 3D FIB-SEM tomography. Subsequently, three high resolution scans (40–60 kV, 3–6.5 W, air or LE filter, 2401 projections over 360° of sample rotation, and 5–14 s exposure time per frame) with a voxel size of $\sim 1\text{--}1.5 \mu\text{m}$ were conducted in selected ROIs using the “Scout & Zoom” function of the microscope, which permitted correlation of X-ray data at various length scales for the same ROI. The tomograms were reconstructed from 2D projections using a Zeiss Microscopy commercial software package (Zeiss NavX 1.0 Control system, Carl Zeiss X-ray Microscopy GmbH, www.zeiss.com/xrm), XMReconstructor (Scout-and-Scan™ Control System Reconstructor – 1.0, Carl Zeiss X-ray Microscopy GmbH, www.zeiss.com/xrm). The reconstructed XRM files were subsequently converted to 8-bit grayscale image stacks and imported into a Dragonfly software program (Dragonfly v 2021.1; Object Research System, Inc., Montreal, Canada, <https://dragonfly.comet.tech/en/product-overview/dragonfly-3d-world>) for volume rendering and visualization. For image segmentation and 3D surface rendering purposes, conversion to 8-bit grayscale images greatly reduces the size of the dataset and allows the analysis to be run on a less powerful workstation. The conversion does not affect the results of segmentation nor visualization. The histogram was not resampled prior to the conversion.

Intermediate correlative microscopy sample preparation

Following the XRM identification of a trabecula situated below the sample surface, the LaserFIB method was again utilized to expose the ROI and prepare the site for PFIB-SEM tomography acquisition (Fig. 1C). The trabecula was chosen because it aligned almost parallel to the sample surface and perpendicular to the edge of the sample block, which minimized the amount of milling of surrounding resin during PFIB-SEM tomography acquisition. For an ROI that was close to the sample surface (less than a few dozens of μm), SEM images of the sample were acquired using Zeiss Atlas 5 software (Zeiss Atlas 5.5.1.75, Carl Zeiss Microscopy GmbH and Fibics Inc., www.fibics.com) and the corresponding XRM dataset was imported into the same workspace. The X-ray dataset was aligned to match the SEM image using the coordinate grid and other surface features which were visible with both imaging modalities. Linking the XRM data to the sample surface in SEM was essential for precise positioning of the laser ablation shapes in the laser CAD software (TruTops Mark CAD 2.12.5.0, Trumpf Schweiz AG, www.zeiss.de/microscopy) in order to account for the positions of deep subsurface specimen features that were not visible in SEM and did not necessarily line up with surface features. The laser processing pattern was also designed to account for the laser beam diameter and typical side wall taper created by LaserFIB ablation.

The LaserFIB site preparation was a two-step process with a coarse ablation step to remove the majority of material in front of the ROI followed by finer ablation steps to approach the ROI precisely, shape the side trenches, and yield a cleaner and flatter cross section. The coarse laser ablation step utilized parameters of 70% maximum power, 150 mm/s velocity, and 20 kHz pulse frequency with 4 bursts in burst-mode, using the cross-jet tool of the LaserFIB to keep the protective glass clean to enable large volume ablation. The fine ablation steps first utilized laser parameters of 25% maximum power, 25 mm/s velocity, and 10 kHz with 4 bursts in burst-mode. This step was followed by a final ablation step to clean the cross section using 15% maximum power, 5 mm/s velocity, and 2.5 kHz pulse frequency with 4 bursts in burst-mode. The fine laser processing steps did not use the cross-jet, in order to yield a result with less debris pile-up on top of the cross section edges.

In areas where the targeted ROIs were deep below the specimen surface—more than $\sim 100 \mu\text{m}$ below—manual grinding and polishing were necessary to remove excessive material from the surface to enable the FIB preparation for PFIB-SEM tomography. This additional step was needed because of the proximity limitations of the gas-injection system nozzle in PFIB-SEM systems to the specimen surface at the coincidence point. Since FIB-induced deposition was essential for PFIB-SEM tomography preparation, attempting to deposit material into deep features beneath the general sample surface necessitated elevating the deep target location to the coincidence height. Doing so, however, would result in a collision between the gas nozzle and the general sample surface level, so grinding down the surface to bring the ROI effectively closer to the surface was a required

intermediate step for deep ROIs. To control the amount of material removed more precisely, the trabecular bone sample was mounted onto a manual specimen holder (Kulzer Technik, Wehrheim, Germany), having a fine adjustment ring with a Vernier scale (distance between two graduations of the scale = 20 μm). The sample was subsequently ground and polished following the same procedure as described previously in Specimen Preparation. The newly exposed bone surface was coated with ~20 nm gold for SEM imaging using the Atlas 5 correlative workspace. The XRM dataset was aligned and linked to the surface in SEM in order to inform the decisions of dimensions and positions for the site-specific LaserFIB processing needed to prepare the ROI for PFIB-SEM tomography, as described above.

Plasma focused ion beam-scanning electron microscope tomography

Following the LaserFIB site preparation, the sample was mounted on a 45° pre-tilt stub holder and loaded into a Helios G4 UXE DualBeam microscope (Thermo Fisher Scientific, Waltham, MA, USA) integrated with a Xenon plasma source for serial “slice and view” image stack acquisition (Fig. 1D). A protective tungsten layer (10–15 μm) was deposited on the sample surface to reduce ion beam damage and curtaining artifacts. Afterwards, fiducials were created on the sample surface and cross section for ion and electron beam image tracking during the acquisition. Finally, each parallel slice of the fine-polished block was milled using a 30 kV ion beam at 15 nA and with a sequentially alternating +/- 5° rocking-polish angle within the parallel plane to reduce curtaining artifacts. After FIB removal of each slice, the freshly exposed cross section encompassing the entire bone trabecular section was imaged with the electron beam at 2 kV acceleration voltage and 400 pA using a retractable concentric backscattered detector (CBS). The slice thickness closely matched the lateral resolution of the SEM images, varying between 60 and 80 nm. Through a fully automated procedure using Auto Slice and View 5 software (Auto Slice & View 5.9, Thermo Fisher Scientific Inc., <https://www.thermofisher.com/ca/en/home/electron-microscopy/products/dualbeam-fib-sem-microscopes/helios-5-pfib-dualbeam.html>), FIB milling was seamlessly integrated with SEM imaging in a sequentially alternating manner — repeating the process of imaging the cross section, then milling away a slice, and reimaging — to capture a stack of hundreds of serial images, in this case 944 images. The image stack underwent alignment (image registration) using the sum of square differences (SSD) method in Dragonfly software (Dragonfly v 2021.1; Object Research System, Inc.) and then removal of background noise. Subsequently, the image stacks were processed for segmentation according to their structural features using a U-net-based deep learning algorithm, and the segmented cellular architecture was visualized in 3D using surface rendering in Dragonfly (v 2021.1, Object Research System, Inc.).

Results and discussion

A LaserFIB-patterned coordinate grid to assist the linking of XRM data to the SEM surface image

A rectangular grid (~7 × 10 mm) with a line spacing of 200 μm was patterned on the entire specimen surface and the surrounding resin using LaserFIB (Fig. 2A). The grid spacing was chosen to strike a balance between accuracy and surface coverage. Additionally, a coordinate system featuring numerical and alphabetical axes was incorporated to facilitate efficient communication among researchers when describing the location of specific trabecular bone features under any grid square (Fig. 2B–E). The grid spacing was comparable to the trabecula thickness and spacing, such that a single trabecula was often adequately contained within one grid space (Fig. 2F–G). The lines, with a thickness of 14 μm and a depth of 10 μm , were distinctly visible in both SEM images (Fig. 2D–E) and XRM micrographs (Fig. 2F–G). An optimized grid depth was necessary to ensure visibility in the XRM data while minimizing FIB curtaining effects from milling across the lines. The ideal grid depth may be slightly less than it was here, perhaps ~4 μm , which is achievable through adjustments in laser power, pulse frequency, or velocity. As a point of interest, a 4 μm grid depth would provide shallower grid lines and thereby reduce curtaining artifacts during “slice and view” of PFIB-SEM tomography. On the other hand, a 4 μm depth should be sufficient to provide a spatial guide in the specimen during high resolution scans. The key for image registration between XRM and SEM is superimposing the high resolution XRM scan in the correlative workspace with the SEM image of the sample surface.

To identify a single trabecula buried deep inside the tissue block and target it with microscale precision, the grid system was integrated into the Zeiss ‘Scout & Zoom’ workflow through X-ray tomographic imaging. The ‘Scout & Zoom’ procedure began with an initial scan of the entire sample followed by progressively higher magnification and resolution scans in targeted areas (Fig. 1B). One particular scan with an imaging resolution of 1.5 μm enabled identification and visualization of a ~100 μm thick, ~600 μm long trabecula from the subsurface region near the edge of the bone sample (ROI, blue, Fig. 3). Based on the XRM scan, this ROI was located between the imaging planes 1.2–1.4 mm below the sample surface (blue-dashed frame, Fig. 3), a depth that is beyond the conventional reach of FIB techniques, including Xe PFIB, as explained in the methodology section (Intermediate correlative microscopy sample preparation). This limitation extended not only to revealing the ROI but also to the site preparation processing for FIB tomography. This process involved FIB-induced deposition of a protective layer and the placement of tracking fiducials, necessitating the location of the ROI to be relatively close to the sample surface level. Therefore, even though a LaserFIB can expose an ROI at this depth, it remains inaccessible for PFIB-SEM tomography.

The location of this deeply subsurface bone ROI with respect to the coordinate grid was clearly identified by projecting the ROI up to the SEM surface level after linking the XRM data within the Atlas software, where the trabecula was situated below four grid cells (blue-shaded bone overlaid by a yellow grid, Fig. 3A). As such, the trabecula coordinate was identified within the 3D space and the structure was further exposed through a combination of manual grinding and polishing followed by LaserFIB processing as described in the Materials and methods section above.

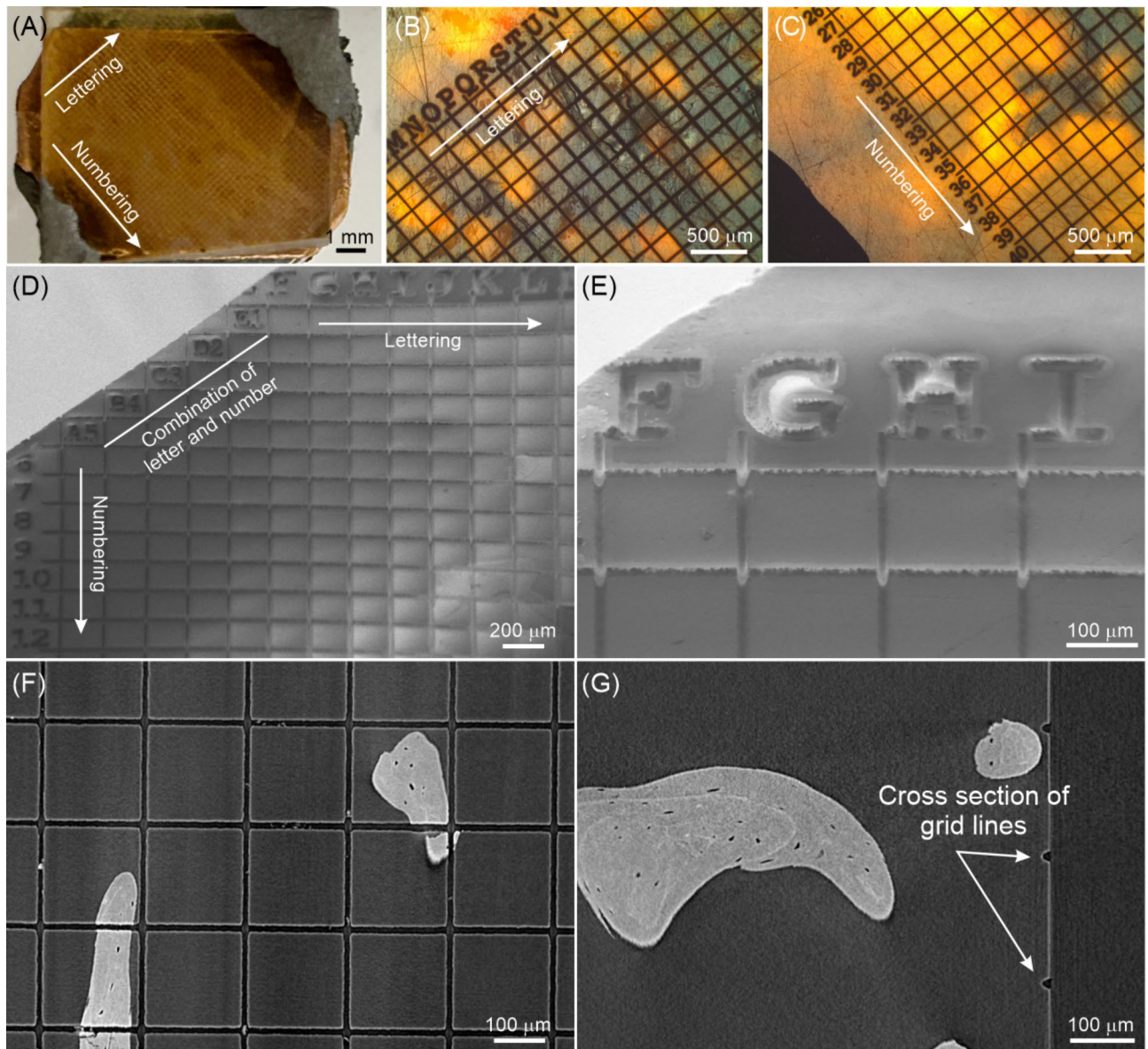


Fig. 2. Coordinate grid markings patterned into the sample surface by the LaserFIB. (A–C) Optical images of the sample surface (A) showing the letter axis (B) and number axis (C) of the grid pattern. (D,E) SEM images of the sample surface at a corner of the coordinate grid depicting the grid markings (D) and at a higher magnification (E) to show the 200 μm grid spacing with a line width of 14 μm . (F,G) X-ray microscopy image slices of a ROI near sample surface level showing the grid in the surface plane (F) and in cross section view (G) of the trabecular bone sample with its mineral (gray/white regions), osteocyte lacunae (small, black holes) and other features.

In recent years, correlative microscopy imaging has become an essential approach to study biological materials, allowing the combination of multiple modalities to examine the structure and properties of precisely the same tissue volume across multiple length scales and dimensions³⁵. An example of such microscopy is correlative light and electron microscopy (CLEM), in which a fluorescence image is overlaid onto an electron microscopy image³⁶. However, identifying and correlating specific ROIs across different imaging modalities in CLEM remains challenging. This difficulty occurs largely because of the complex process of transforming sample coordinates for comparison across various microscopes, which demands extensive expertise to identify common features in multiple images. In this regard, creating fiducial markers, either intrinsic or extrinsic to the sample, can help circumvent the problem of co-registration of images. Various markers have been introduced in the past in CLEM, including scratches and computer-readable image pointers³⁷, particles and fluorophores³⁸. In particular, one method used a femtosecond pulsed titanium sapphire laser to create defined fiducial markers in 3D in fixed tissue³⁹. These markers were autofluorescent and generated electron contrast, which was visible under both light and electron microscopy³⁹.

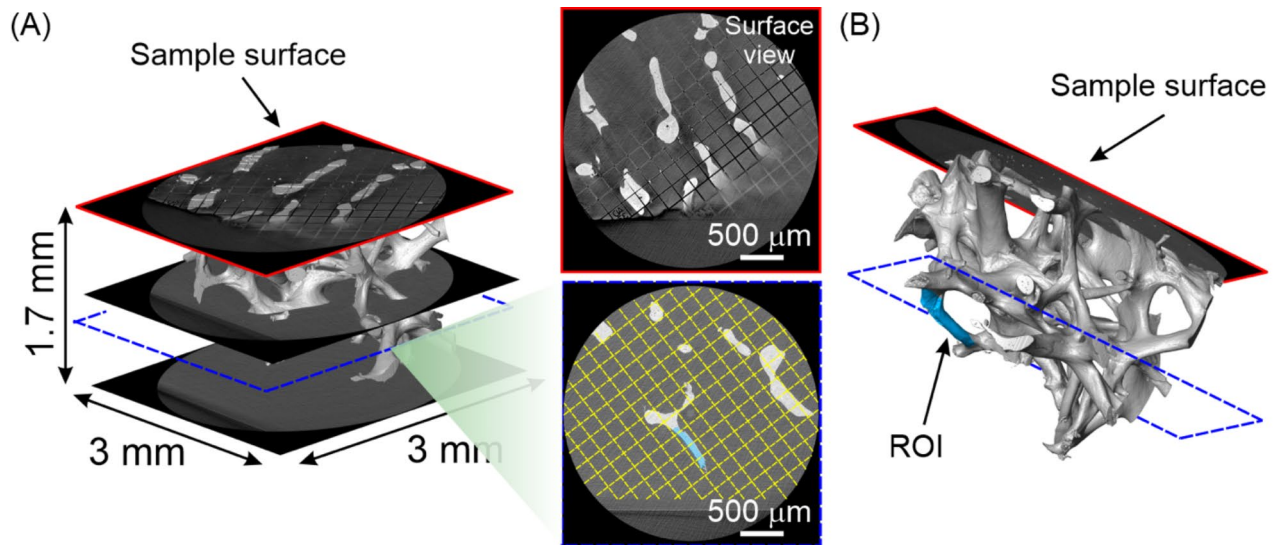


Fig. 3. X-ray tomography of a human trabecular bone sample. **(A)** 3D volume rendering of a portion of trabecular bone tissue intersected by three XRM imaging planes, 3×3 mm and separated by ~ 0.85 mm each. Two selected XRM images corresponding to the same volume are shown, one of which is the sample surface, outlined by red solid lines where the surface grid is visible. The other is an XRM image beneath the sample surface (blue-dashed lines) superimposed virtually with the grid (yellow lines) showing the relative location of the ROI (blue-shaded area) within the sample. **(B)** 3D volume rendering of trabecular bone from the same sample of **(A)** intersected by the surface imaging plane (red solid lines) revealing the ROI (blue-shaded volume) beneath the sample surface corresponding to the ROI in **(A)**.

In contrast to the previous studies primarily focused on CLEM, we have established a unique image registration system capable of correlating a 3D image dataset of human trabecular bone acquired by XRM and electron microscopy at different length scales. This methodology facilitates navigation to the surface projection of any specific subsurface ROI, enabling imaging and characterization of subsurface details across multiple length scales that no single technique can achieve alone. Our system features a custom-designed laser-patterned coordinate grid with precisely spaced alphanumeric axes (Fig. 2), providing a sample-wide framework for efficient communication of any ROIs within the sample in 3D space. By specifying the surface-level grid cell coordinates and the depth of the ROI below them, researchers can precisely target ROIs using FIB or LaserFIB methods, as demonstrated in the present work. Even for ROI targets that are significantly smaller than the grid spacing, their precise locations can be effectively communicated by describing micron-scale distances, measurable from the XRM data, to the sides or corners of any given grid cell. While similar approaches using XRM alone^{32,33,40} or in combination with laser-patterned rulers to target subsurface features in bulk materials have been reported before⁴¹, our approach with a laser-patterned coordinate grid offers a much more comprehensive communication system through its full-sample coverage and alphanumerically labelled axes. The laser ablation process described herein is efficient, requiring minimal ablation time of 80 s in this case, and can be tailored to accommodate various grid spacings, rotations, and specimen shapes within the 40×40 mm LaserFIB scan field.

By integrating the 3D data generated from the XRM into a correlative workflow, we have identified subsurface ROIs and estimated the amount of surface material for removal. The precise removal of sample material in the correlative workflow to expose inner ROIs is a complex process. On consideration of sample composition, amount of material to be removed, and accuracy of material removal, various approaches can be utilized, including manual and/or automated grinding and polishing, microtomy or ultramicrotomy, broad-beam ion milling, serial block face-scanning electron microscopy, Xe PFIB-SEM, and LaserFIB ablation⁴². In the current study, for ROIs that were hundreds of μm or mm beneath the sample surface (for example, Fig. 3), manual polishing was adopted to remove large amounts of surface material in a cost-effective way (Fig. S1). The polishing depth was controlled to an accuracy of ~ 20 μm by the fine adjustment ring of a polishing holder with a Vernier scale (Fig. S1). Once an estimated amount of surface material was removed, the newly exposed sample surface was again examined under SEM and correlated with XRM data through Atlas 5 software (Fig. S2). Subsequently, the specific areas of interest in the sample were targeted more precisely with LaserFIB and exposed in preparation for PFIB-SEM tomography.

Human trabecular bone structure in 3D revealed by high resolution XRM

The XRM ‘Scout & Zoom’ function was used to generate high resolution local tomographic scans of subsurface ROIs and revealed features within a small trabecular bone tissue volume (Fig. 4). Dozens of osteocyte lacunae of various sizes appeared as dark holes and most of them seemed to be elongated along the direction of the long axis of the trabecula. A few lacunae were observed in areas with relatively lower grayscale values compared to the adjacent bone tissue matrix that was examined, an observation suggesting an early stage of mineralization. There was no apparent lamellar bone structure, possibly because of the limited contrast and the utilization of a

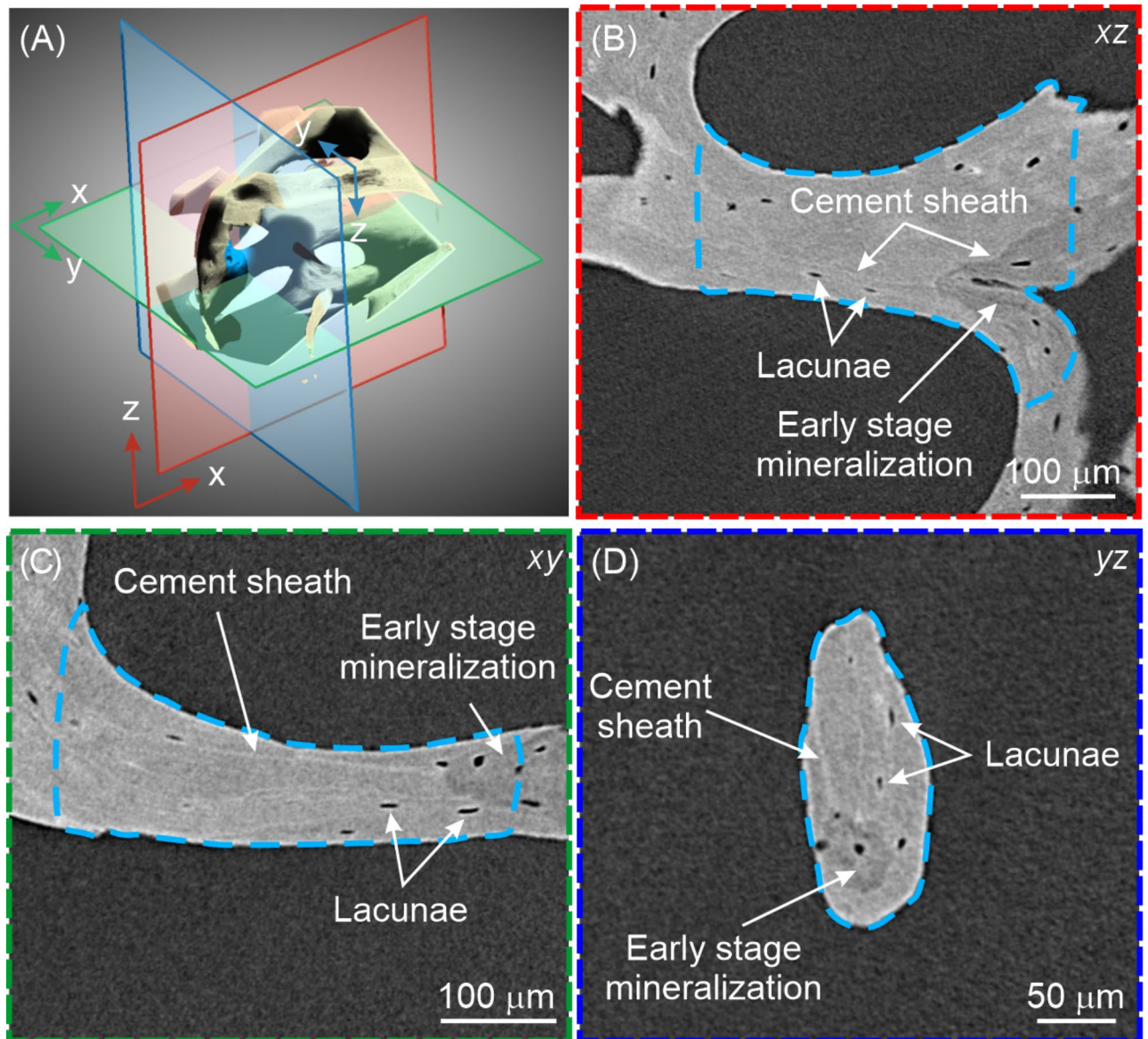


Fig. 4. High resolution X-ray tomography of a small trabecular bone tissue volume examined through the use of the 'Scout & Zoom' function with a voxel size of 1.5 μm . (A) 3D volume rendering of the selected trabecular bone region superimposed by three intersecting mutually orthogonal planes (red, green and blue) with their corresponding coordinates. A selected ROI is highlighted in blue. (B–D) XRM images from the three orthogonal planes in (A) showing bright cement sheaths, osteocyte lacunae and regions with relatively lower grayscale values in the trabecular bone tissue. The selected ROI is outlined by blue-dashed lines.

polychromatic beam in the laboratory-based X-ray setting. It is worth noting that several bright cement sheaths were found along the direction of the trabecula long axis, one of which delineated an early stage mineralizing bone structural unit.

Instrumentation for laboratory-based 3D X-ray imaging has seen remarkable developments in the past few decades. In this regard, the recent advances in XRM (for example, Zeiss XRM Resolution at a Distance, Raad™) featuring dual-stage magnification based on synchrotron-caliber optics can achieve submicron resolution at large working distances⁴³, one of the key advantages of the method over traditional micro-CT. This result was demonstrated in the present study where high resolution XRM revealed fine trabecular bone structural features, including cell lacunae in various sizes $\sim 10\text{--}20\ \mu\text{m}$. It is well known that osteocytes in human bone play an important role in bone remodeling and mineral homeostasis⁴⁴. Changes in lacunar shape and density of these cells have been associated with aging⁴⁵ and conditions such as lactation-induced bone loss, osteopenia, osteoporosis and osteoarthritis^{46,47}. The current study found more rounded and larger osteocyte lacunae in areas with lower grayscale values, which are typically interpreted as indications of early stage mineralization. This observation is in line with previous studies in human showing larger osteocytes in woven bone⁴⁸, as well as infantile cortical⁴⁹ and trabecular bone⁵⁰.

The cement sheath is another feature examined by high resolution XRM. The cement sheath is a thin layer of material in human trabecular bone that separates newer bone structural units from older interstitial bone. Although the precise composition, function, and other aspects of the cement sheath are still incompletely understood^{51,52}, it is recognized as holding an important role in bone deformation and fracture by arresting and/or deflecting microcrack propagation^{53–55}. Because of the narrow width of the cement sheaths (less than 5 μm) in the trabecular bone sample investigated here, it would be impossible to visualize and analyze this structural component using older generation laboratory-based micro-CT techniques. Here, we demonstrated the possibility of using laboratory-based XRM to distinguish cement sheaths, which appeared brighter and with higher grayscale values compared to the remainder of the bone tissue. These results are indications that cement sheaths contain a higher mineral content compared with that of lamellar bone, a conclusion supporting previous studies using quantitative backscattered electron imaging^{56,57}, Raman spectroscopy⁵⁶, energy-dispersive X-ray spectroscopy⁵⁷, and X-ray fluorescence tomography⁵⁸. That being said, recent studies using high resolution FIB-SEM imaging have challenged the traditional view of cement sheath mineralization at the nanometer length scale^{19,21}.

Site-specific LaserFIB ablation through the correlative workspace

The 3D XRM dataset was imported into the Zeiss Atlas 5 correlative workspace, where 2D slices of the data at the surface level were superimposed and aligned with the SEM image of the sample surface. This process linked and synchronized the XRM data with the current SEM coordinate system (Fig. S2). This alignment enabled the accurate display of subsurface 2D XRM slices with respect to their locations, revealing target ROIs to assist in precise placement decisions for subsequent LaserFIB and PFIB-SEM processing toward further nanoscale imaging and characterization techniques.

As demonstrated in Fig. 5, distinctive osteocyte lacunae with varying shapes were identified at the surface level within the selected trabecula (Fig. 5A) from the XRM dataset (Fig. 5B, arrowheads). These structural characteristics were cross-referenced with those observed through live SEM imaging (Fig. 5C, arrowheads) to define the target area for PFIB-SEM tomography. Subsurface 2D slices of the XRM data were also utilized to refine and delineate the tomography volume more precisely by determining the depth of the trabecula and projecting its subsurface shape toward the surface. This step is essential because it cannot be assumed that the boundaries of the surface-level features as observed by SEM will extend straight downward from the surface.

Following the registration of stage positions for the ROI and the fiducials on the laser sample holder and the positioning of ROIs on the stage, the sample was transferred to the integrated laser processing airlock chamber that was separate from the FIB-SEM chamber. This separation protected the instrument columns and detectors from contamination by debris generated by laser ablation. Subsequently, a large trench was milled to provide SEM imaging access orthogonally from the edge direction to the targeted bone structure beneath the sample surface (Fig. 5D). The quality of the laser-prepared cross section was sufficient to recognize cell lacunae within the trabecula, and the SEM image was aligned with a cross section image from the XRM data (Fig. 5E).

The advantages of using Ga- or Xe-based FIB to prepare site-specific cross sections of samples are well known: the nanoscale resolution of FIB gives the system the capability for precision cutting with positional placement accuracy on the order of the diameter of the ion beam^{59,60}. Additionally, this property allows FIB to be used routinely to produce thin TEM lamellae from specific locations of bulk materials, such as from tissue samples or large cells from multicellular organisms^{61,62}. While Ga and Xe FIB preparation has paved the way for tomographic imaging by serial sectioning, the sample volumes that may be extracted and imaged are small compared to the removal capability of an fs laser.

An fs laser has been traditionally employed in studying metallic materials^{63,64}, but this technique has recently attracted growing interest for biological materials processing in clinical and biomedical research^{34,65–67}. The increased use and application of the fs laser are largely attributable to its ultrashort laser pulse duration, which results in limited penetration depth of the thermal diffusion zone in the material⁶⁸. The small heat-affected zone allows for a much closer positioning to the edges of target ROIs than previously feasible with nano- and picosecond lasers, significantly broadening the scope of potential applications for lasers in micro- and nanoscale materials characterization. This specific property is of extreme importance when considering the interaction of the laser beam with biological materials to minimize mechanical and thermal damage to the tissue. Therefore, for beam-sensitive materials, fs laser processing may offer a less damaging option compared to high-current FIB milling for exposing cross sections, fabrication of microscale structures, and preparing sites for FIB-SEM tomography.

Another major advantage of fs laser processing over conventional Ga or Xe FIB milling is its rapid ability to remove substantial material volumes. As noted previously, the ablation process for the 10×7 mm coordinate grid pattern utilized here required only 80 s with the LaserFIB, while the coarse and fine ablation steps for PFIB-SEM tomography preparation each took approximately 90 s. In contrast, completing the same preparation with a Xe PFIB would take significantly longer (estimated to be on the order of hours) and would subject the sensitive resin and bone material to relatively high ion beam currents.

Although the high-precision and high-quality ablation feature of the fs laser has led to its broad application in laser surgery experiments within single cells, as well as within intact organisms^{65–67}, there have been few studies using the instrument to prepare and process biological materials³⁰. Deerinck et al. explored the potential of using the fs laser for large volume machining and electron microscopy imaging of mouse colon tissue⁶⁹. In another study, Bosch et al. demonstrated a workflow to extract multiple pillar-shaped micrometer-sized samples from a resin-embedded mouse olfactory bulb glomerulus³⁴, a result that highlighted the advantage of using the fs laser in biological sample preparation compared to conventional methods such as ultramicrotomy⁷⁰. In the current study, the LaserFIB was directly guided by the XRM dataset (Fig. 5B–E) to prepare the ROIs in human trabecular bone for PFIB-SEM tomography acquisition (Fig. 5D) with minimal damage or artefacts.

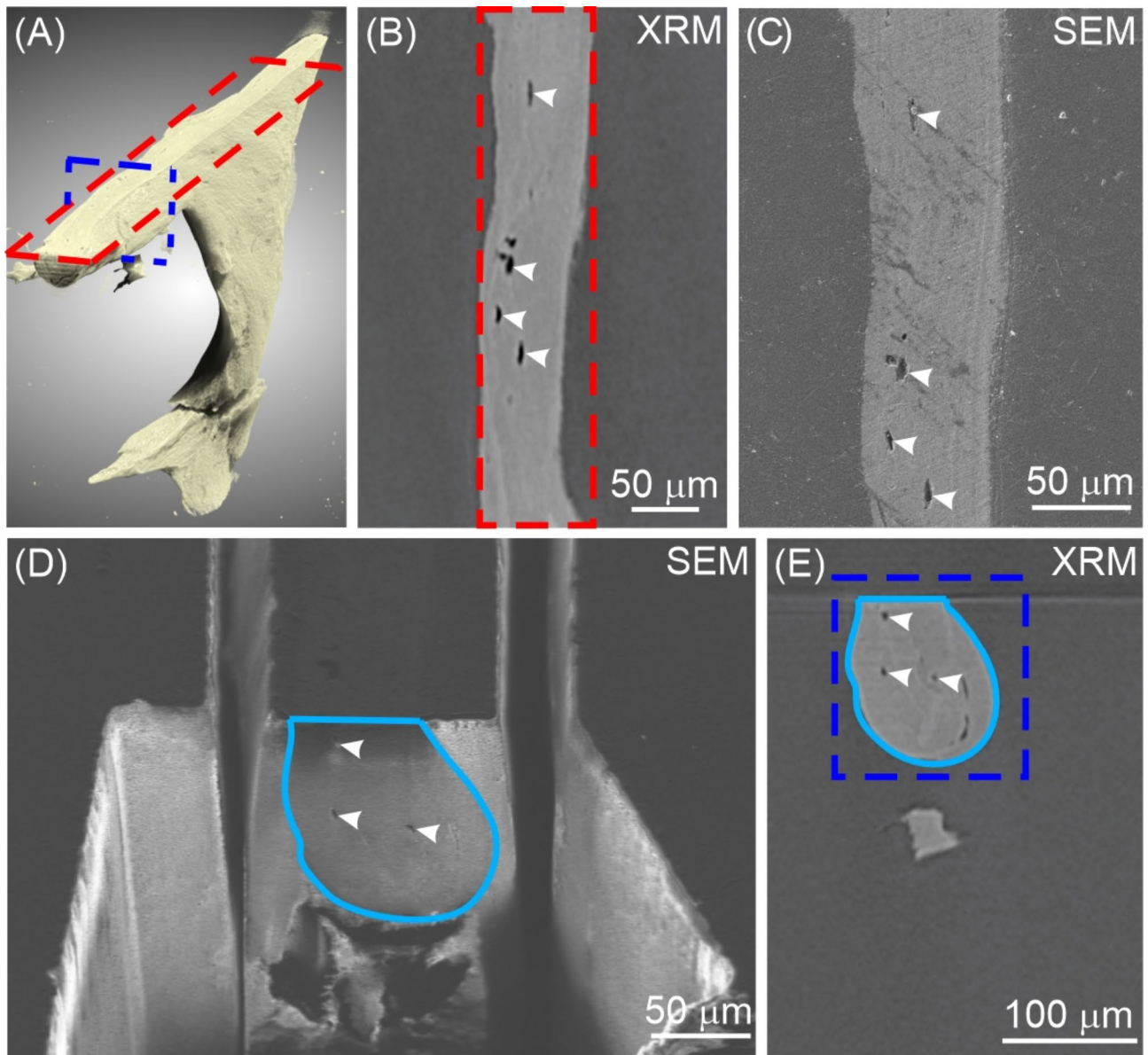


Fig. 5. Correlation between XRM data and LaserFIB processing. **(A)** 3D volume rendering of a small region of trabecular bone superimposed by two intersecting orthogonal planes (blue and red). **(B)** An XRM image slice from the imaging plane indicated by the red-dashed frame in **(A)** showing several distinct osteocyte lacunae (arrowheads). **(C)** The lacunae in **(B)** as observed in the corresponding live SEM image of the sample surface (arrowheads). **(D)** A tilted-view SEM image of the trabecular bone cross section (solid blue line) showing several osteocyte lacunae (arrowheads). The cross section was prepared by site-specific LaserFIB processing through linking the XRM data to the live SEM image using the correlative workspace of the Atlas 5 software. **(E)** An XRM image of the same cross section revealed by the laser in **(D)** showing corresponding osteocyte lacunae (arrowheads) within the bone tissue volume (solid blue line).

This approach demonstrates the rapid and precise ablation and removal of embedded biological material on the scale of hundreds of micrometers using the LaserFIB, and its application could extend to the microscopic characterization of a wide variety of materials, even into millimeter length scales.

PFIB-SEM tomography imaging of human trabecular bone

Based on the high resolution XRM scan of a single trabecula (Fig. 6A), a stack of serial PFIB-SEM images was acquired from a bone subvolume with a resolution of ~ 60 nm and a tissue volume of $\sim 100 \times 100 \times 75 \mu\text{m}^3$ (Figs. 6B and 7 and Movie S1). The PFIB-SEM imaging plane was normal to the long axis of the trabecula, and the field of view encompassed nearly the entire cross section of the trabecula (Fig. 6B). Comparing the micrographs obtained at approximately the identical locations along the trabecula long axis using XRM (Fig. 6A) and PFIB-SEM (Fig. 6B), the images were matched through several unique structure features, including the bright cement

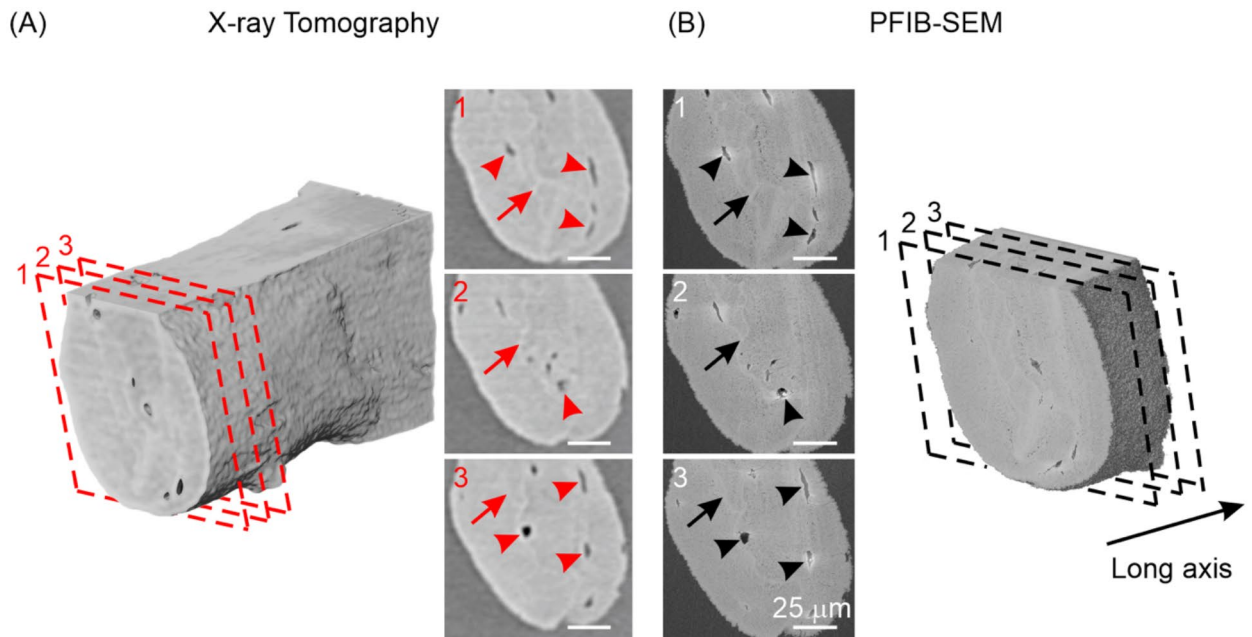


Fig. 6. Correlation between XRM data and PFIB-SEM images. **(A)** 3D volume rendering of a trabecula examined by XRM and three XRM images obtained from corresponding imaging planes (red-dashed frames) superimposed on the trabecula. Multiple cell lacunae (red arrowheads) and cement sheaths (red arrows) are visible in the XRM images. **(B)** 3D PFIB-SEM volume rendering of the identical trabecula region shown in **(A)** and three PFIB-SEM images obtained from the same respective volumes examined in **(A)**. The cell lacunae (black arrowheads) and cement sheaths (black arrows) observed by PFIB-SEM imaging **(B)** are correlated with those (red arrowheads and black arrows) observed by XRM tomography **(A)**.

sheaths traversing the tissue in irregular paths and the distinctly shaped cell lacunae embedded within the bone matrix. The cell lacunae appeared generally to be elongated in the tissue cross sections and along the direction parallel to the surface outline of the trabecular bone.

The major difference between the XRM and PFIB-SEM images was the improved resolution in the SEM images. In SEM, cell lacunae had sharper borders, the bone structure units were clearly defined by the bright cement sheaths, and fine structural details that were beyond the detection limit of XRM became visible (Figs. 6B and 7A). More specifically, micrometer-long and dark canaliculi radiating from the cell lacunae could be observed. Some canaliculi were found to be directly connecting the lacunae with the bone surface (Fig. 7a). Similar observations regarding the directionality of canaliculi have been made in our own as well as other previous studies at the bone-implant interface^{71,72} and in demineralized trabecular bone⁷³. Additionally, micrometer-sized mineral ellipsoids were evident in the PFIB-SEM images (Fig. 7b). This structure unit was reported recently by this laboratory through the use of PFIB-SEM imaging of human cortical bone¹⁷ and bone-implant interfaces⁷¹. Mineral ellipsoids have also been found in healthy and diseased mouse bones¹⁶ and the mouse entheses⁷⁴. From the PFIB-SEM data we obtained, cell lacunae were segmented and presented in 3D within the trabecular bone under investigation (Fig. 7B,C). The 3D surface rendering provided a more complete picture of the shape of the lacunae, appearing flattened with their long axis aligned with the trabecular bone long axis.

Many imaging modalities have been developed to investigate complex bone structure features in 3D at the micro-, meso-, and nanoscales. Among these techniques, XRM⁸, synchrotron radiation nano-CT (SRnCT)^{58,75–77}, and FIB-SEM tomography⁷⁸ have emerged as powerful tools to reveal fine structure details, such as the osteocyte network. Suniaga et al. used XRM to study zebrafish vertebrae and quantified the preferred orientation, sphericity, and volume of the osteocyte lacunae⁷⁹. In a comprehensive review of bone X-ray tomography studies, Wittig et al. demonstrated XRM characterization of the orientation and shape of osteocyte lacunae in mouse femoral cortical bone⁸. With a typical resolution of 30–100 nm, SRnCT is capable of quantifying the branching properties and number of canaliculi in relation to lacunae within a smaller field of view^{77,80,81}. FIB-SEM tomography has also been used in several studies to visualize canaliculi together with osteocyte lacunae as this method possesses resolution sufficient to resolve the small canaliculi at the nanoscale^{16,19,20,73,82}. However, the limited milling rates for traditional Ga FIB impose practical restrictions on the maximum length scale that can be examined, resulting in only portions of lacunae being captured, albeit with a high resolution. PFIB-SEM overcomes the length scale constraints of Ga FIB-SEM, extending into the range of tens and hundreds of micrometers. PFIB-SEM can be an effective complement to XRM for enhancing the resolution of features within dataset volumes at the lower end of the typical XRM length scale range, especially when the finest resolution of Ga FIB-SEM tomography is not essential. In recent work from this laboratory investigating human cortical bone¹⁷ and bone-implant interfaces⁷¹, the advantages of Xe PFIB-SEM were highlighted with its faster milling rates and accessibility to larger volume

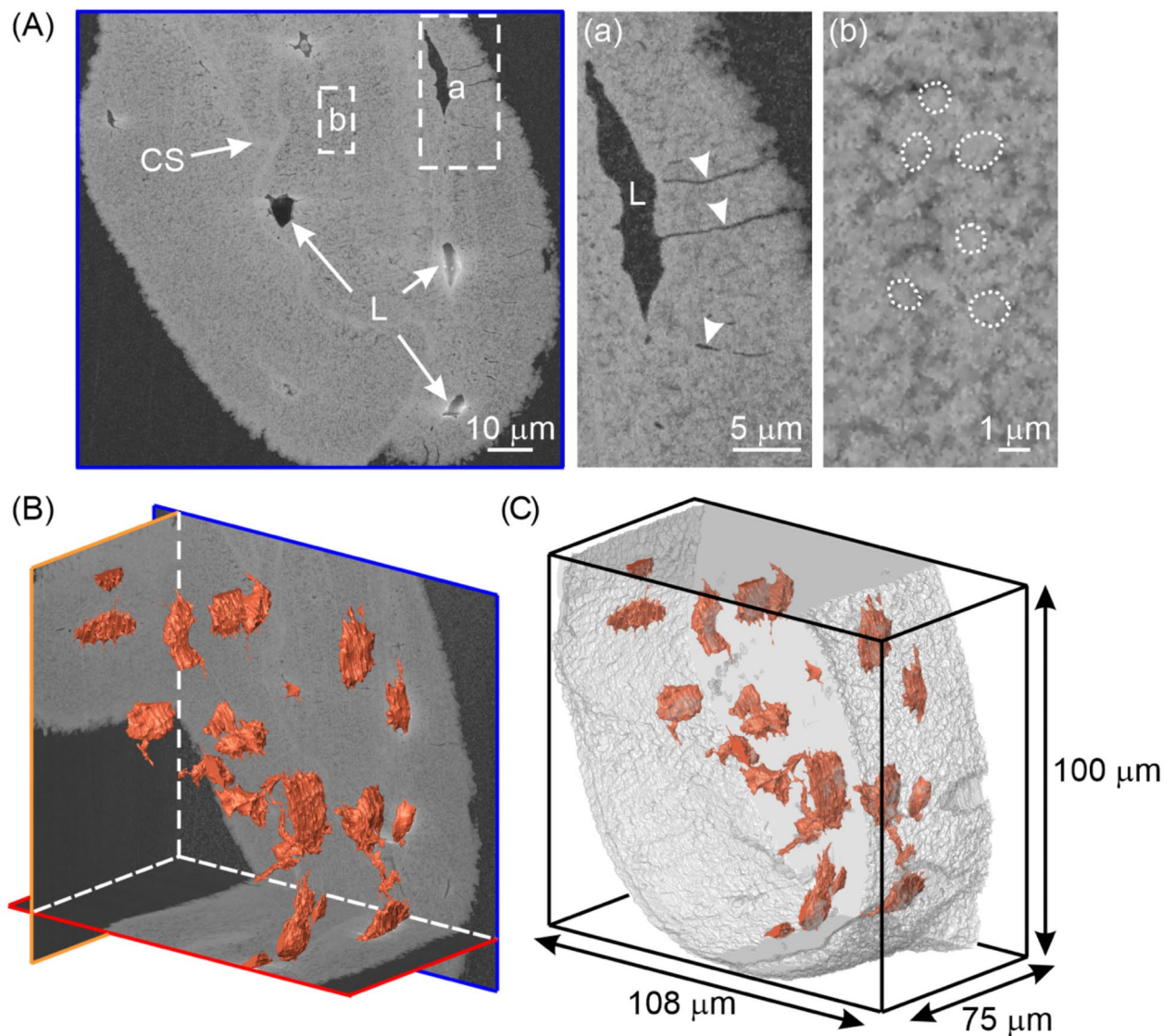


Fig. 7. PFIB-SEM examination of a region from a trabecula. (A) A representative backscattered electron image acquired from the stack of the PFIB-SEM images. Bright cement sheaths (CS) and elongated cell lacunae (L) are clearly visible. Fine trabecular bone structure features including canaliculi radiating from a lacuna (arrowheads) and mineral ellipsoids (dotted circles) are shown in the two enlarged backscattered electron images (a) and (b), respectively. (B) 3D volume rendering of cell lacunae (tangerine) in the trabecular bone and depicted with three intersecting mutually orthogonal planes in the background. (C) 3D surface rendering of the trabecular bone (transparent gray) and its embedded cell lacunae (tangerine) distributed throughout an imaged region measuring $108 \times 75 \times 100 \mu\text{m}$. Bright rims along the edges of lacunae shown in (A) are a result of specimen charging during examination.

analysis while maintaining acceptable nanoscale SEM resolution. In the current study with PFIB-SEM, the entire cross section of a trabecula was captured with a volume that exceeded $100 \mu\text{m}^3$ (Figs. 6 and 7). More importantly, by directly linking XRM and PFIB-SEM data (Fig. 6), this study demonstrated the potential for accurate and higher resolution characterization of local regions of bone structure within the context of the much greater tissue volumes that can be more broadly characterized by XRM. This precise correlative approach can be further utilized to identify bone trabeculae at various stages of development and growth. The methodology can also be used to locate and identify trabeculae that are aligned with distinct stress trajectories. In this regard moreover, the workflow can help define bone structural architecture affected by biomechanical factors across the wide spectrum of length scales from the gross anatomical level to meso- and nanoscale levels. Even more broadly, this approach can be employed to study developmental biology to examine tissue growth across the same multiple length scales.

Conclusion

The present work highlights the advantages and novelty of using multiscale and multimodal correlative microscopy to examine human trabecular bone structure. It enables the targeting of specific subsurface ROIs deeply buried inside the sample for detailed morphological analysis. With LaserFIB patterning of a coordinate grid, we were able to create a reliable correlation system where a trabecula containing cement sheaths and cell lacunae could be easily visualized, and the precise location of the trabecula relative to the surface coordinate grid could be identified and easily communicated using XRM scans in combination with SEM surface-level targeting. The LaserFIB can efficiently and precisely uncover large area cross sections of the sample to facilitate subsequent PFIB-SEM tomography acquisition, which revealed detailed cellular morphology and cement sheath structure. The methodologies demonstrated in this work can be applied across their wider range of length scales to other fields of materials characterization beyond biomaterials, such as traditionally engineered materials, semiconductor devices, and geological specimens. This workflow provides the potential to address complex research questions that require a correlative tomographic analysis over various length scales, an approach which will improve our understanding of the structural hierarchy in a host of materials and yield valuable insight for mimicking natural structures and developing new engineering constructs.

Data availability

All the imaging data and 3D segmentations and renderings from the current study are available from the corresponding author upon request.

Received: 11 April 2024; Accepted: 10 September 2024

Published online: 16 September 2024

References

- Weiner, S. & Wagner, H. D. The material bone: Structure-mechanical function relations. *Annu. Rev. Mater. Sci.* **28**, 271–298 (1998).
- Fratzl, P., Gupta, H. S., Paschalis, E. P. & Roschger, P. Structure and mechanical quality of the collagen–mineral nano-composite in bone. *J. Mater. Chem.* **14**, 2115–2123 (2004).
- Fratzl, P. & Weinkamer, R. Nature's hierarchical materials. *Prog. Mater. Sci.* **52**, 1263–1334 (2007).
- Buss, D. J., Kröger, R., McKee, M. D. & Reznikov, N. Hierarchical organization of bone in three dimensions: A twist of twists. *J. Struct. Biol.* **X** **6**, 100057 (2021).
- Reznikov, N., Shahar, R. & Weiner, S. Bone hierarchical structure in three dimensions. *Acta Biomater.* **10**, 3815–3826 (2014).
- Shah, F. A., Ruscsák, K. & Palmquist, A. 50 years of scanning electron microscopy of bone—A comprehensive overview of the important discoveries made and insights gained into bone material properties in health, disease, and taphonomy. *Bone Res.* **7**, 15 (2019).
- Grandfield, K. et al. Atom probe tomography for biomaterials and biomineralization. *Acta Biomater.* **148**, 44–60 (2022).
- Wittig, N. K. et al. Opportunities for biomineralization research using multiscale computed X-ray tomography as exemplified by bone imaging. *J. Struct. Biol.* **214**, 107822 (2022).
- Georgiadis, M., Müller, R. & Schneider, P. Techniques to assess bone ultrastructure organization: Orientation and arrangement of mineralized collagen fibrils. *J. R. Soc. Interface* **13**, 20160088 (2016).
- Suuronen, J. P., Hesse, B., Langer, M., Bohner, M. & Villanova, J. Evaluation of imaging setups for quantitative phase contrast nanoCT of mineralized biomaterials. *J. Synchrotron Radiat.* **29**, 843–852 (2022).
- Sauer, K. et al. Primary radiation damage in bone evolves via collagen destruction by photoelectrons and secondary emission self-absorption. *Nat. Commun.* **13**, 7829 (2022).
- Ciani, A. et al. Ptychographic X-ray CT characterization of the osteocyte lacuno-canalicular network in a male rat's glucocorticoid induced osteoporosis model. *Bone Rep.* **9**, 122–131 (2018).
- Reznikov, N., Bilton, M., Lari, L., Stevens, M. M. & Kröger, R. Fractal-like hierarchical organization of bone begins at the nanoscale. *Science* **360**, eaao2189 (2018).
- Grandfield, K., Vuong, V. & Schwarcz, H. P. Ultrastructure of bone: hierarchical features from nanometer to micrometer scale revealed in focused ion beam sections in the TEM. *Calcif. Tissue Int.* **103**, 606–616 (2018).
- Micheletti, C. et al. From tissue retrieval to electron tomography: Nanoscale characterization of the interface between bone and bioactive glass. *J. R. Soc. Interface* **18**, 20210181 (2021).
- Buss, D. J., Reznikov, N. & McKee, M. D. Crossfibrillar mineral tessellation in normal and hyp mouse bone as revealed by 3D FIB-SEM microscopy. *J. Struct. Biol.* **212**, 107603 (2020).
- Binkley, D. M., Deering, J., Yuan, H., Gourrier, A. & Grandfield, K. Ellipsoidal mesoscale mineralization pattern in human cortical bone revealed in 3D by plasma focused ion beam serial sectioning. *J. Struct. Biol.* **212**, 107615 (2020).
- Raguin, E., Rechav, K., Brumfeld, V., Shahar, R. & Weiner, S. Unique three-dimensional structure of a fish pharyngeal jaw subjected to unusually high mechanical loads. *J. Struct. Biol.* **211**, 107530 (2020).
- Raguin, E., Rechav, K., Shahar, R. & Weiner, S. Focused ion beam-SEM 3D analysis of mineralized osteonal bone: Lamellae and cement sheath structures. *Acta Biomater.* **121**, 497–513 (2021).
- Tang, T. et al. A 3D network of nanochannels for possible ion and molecule transit in mineralizing bone and cartilage. *Adv. NanoBiomed. Res.* **2**, 2100162 (2022).
- Tang, T. et al. Subcanalicular nanochannel volume is inversely correlated with calcium content in human cortical bone. *J. Bone Min. Res.* **38**, 313–325 (2023).
- Landis, W. J., Hodgens, K. J., Arena, J., Song, M. J. & McEwen, B. F. Structural relations between collagen and mineral in bone as determined by high voltage electron microscopic tomography. *Microsc. Res. Tech.* **33**, 192–202 (1996).
- Liebi, M. et al. Nanostructure surveys of macroscopic specimens by small-angle scattering tensor tomography. *Nature* **527**, 349–352 (2015).
- Georgiadis, M. et al. Ultrastructure organization of human trabeculae assessed by 3D sSAXS and relation to bone microarchitecture. *PLoS One* **11**, e0159838 (2016).
- Morrell, A. P. et al. Addressing uncertainties in correlative imaging of exogenous particles with the tissue microanatomy with synchronous imaging strategies. *Metallomics* **15**, mfa030 (2023).
- Zhu, Y., Manske, S. L. & Boyd, S. K. Cartilage imaging of a rabbit knee using dual-energy X-ray microscopy and 1.0 T and 9.4 T magnetic resonance imaging. *J. Orthop. Transl.* **3**, 212–218 (2015).
- Merkle, A. P. & Gelb, J. The ascent of 3D X-ray microscopy in the laboratory. *Microsc. Today* **21**, 10–15 (2013).
- Burnett, T. L. et al. Correlative tomography. *Sci. Rep.* **4**, 4711 (2014).

29. Echlin, M. P., Burnett, T. L., Polonsky, A. T., Pollock, T. M. & Withers, P. J. Serial sectioning in the SEM for three dimensional materials science. *Curr. Opin. Solid State Mater. Sci.* **24**, 100817 (2020).
30. Tordoff, B. et al. The LaserFIB: New application opportunities combining a high-performance FIB-SEM with femtosecond laser processing in an integrated second chamber. *Appl. Microsc.* **50**, 24 (2020).
31. Sugioka, K. & Cheng, Y. Ultrafast lasers—Reliable tools for advanced materials processing. *Light Sci. Appl.* **3**, e149 (2014).
32. Kelly, S. T. et al. Correlated XRM and 3D FIB-SEM workflow to investigate the structure-property relationship of Si-based battery anode materials. *Microsc. Microanal.* **28**, 198–199 (2022).
33. Harris, W. *Multi-scale correlative study of corrosion evolution in a magnesium alloy*. *Carl Zeiss Microscopy Applicatin Note* (2015).
34. Bosch, C. et al. Femtosecond laser preparation of resin embedded samples for correlative microscopy workflows in life sciences. *Appl. Phys. Lett.* **122**, 143701 (2023).
35. Loussert Fonta, C. & Humbel, B. M. Correlative microscopy. *Arch. Biochem. Biophys.* **581**, 98–110 (2015).
36. Tanner, H., Sherwin, O. & Verkade, P. Labelling strategies for correlative light electron microscopy. *Microsc. Res. Tech.* **86**, 901–910 (2023).
37. Sheriff, J., Fletcher, I. W. & Cumpson, P. J. Computer-readable image markers for automated registration in correlative microscopy – autoCRIM. *Ultramicroscopy* **228**, 113322 (2021).
38. Mohammadian, S. et al. High accuracy, fiducial marker-based image registration of correlative microscopy images. *Sci. Rep.* **9**, 3211 (2019).
39. Bishop, D. et al. Near-infrared branding efficiently correlates light and electron microscopy. *Nat. Methods* **8**, 568–570 (2011).
40. Johnson, G. M., Hartfield, C., Mueller, S. & Kaestner, M. New physical analysis capability for counterfeit electronics and reverse engineering. In *IEEE Physical Assurance and Inspection of Electronics (PAINE)* 1–5 (IEEE, 2020).
41. Viswanathan, V. & Jiao, L. Developments in advanced packaging failure analysis using correlated X-Ray microscopy and LaserFIB. In *IEEE 23rd Electronics Packaging Technology Conference (EPTC)* 80–84 (IEEE, 2021).
42. Mitchell, R. L. et al. Methods to expose subsurface objects of interest identified from 3D imaging: The intermediate sample preparation stage in the correlative microscopy workflow. *J. Microsc.* **289**, 107–127 (2023).
43. Villarraga-Gómez, H. et al. Assessing rechargeable batteries with 3D X-ray microscopy, computed tomography, and nanotomography. *Nondestruct. Test. Eval.* **37**, 519–535 (2022).
44. Bonewald, L. F. The amazing osteocyte. *J. Bone Min. Res.* **26**, 229–238 (2011).
45. Tiede-Lewis, L. M. & Dallas, S. L. Changes in the osteocyte lacunocanalicular network with aging. *Bone* **122**, 101–113 (2019).
46. van Hove, R. P. et al. Osteocyte morphology in human tibiae of different bone pathologies with different bone mineral density—Is there a role for mechanosensing? *Bone* **45**, 321–329 (2009).
47. Qing, H. et al. Demonstration of osteocytic perilacunar/canalicular remodeling in mice during lactation. *J. Bone Min. Res.* **27**, 1018–1029 (2012).
48. Hernandez, C. J., Majeska, R. J. & Schaffler, M. B. Osteocyte density in woven bone. *Bone* **35**, 1095–1099 (2004).
49. Zimmermann, E. A. et al. Mechanical competence and bone quality develop during skeletal growth. *J. Bone Min. Res.* **34**, 1461–1472 (2019).
50. Jandl, N. M. et al. Large osteocyte lacunae in iliac crest infantile bone are not associated with impaired mineral distribution or signs of osteocytic osteolysis. *Bone* **135**, 115324 (2020).
51. McKee, M. D. & Nanci, A. Osteopontin at mineralized tissue interfaces in bone, teeth, and osseointegrated implants: Ultrastructural distribution and implications for mineralized tissue formation, turnover, and repair. *Microsc. Res. Tech.* **33**, 141–164 (1996).
52. McKee, M. D. & Nanci, A. Osteopontin and the bone remodeling sequence. *Ann. N. Y. Acad. Sci.* **760**, 177–189 (1995).
53. Kennedy, O. D. et al. The effects of increased intracortical remodeling on microcrack behaviour in compact bone. *Bone* **43**, 889–893 (2008).
54. Tang, T. et al. Shear deformation and fracture of human cortical bone. *Bone* **71**, 25–35 (2015).
55. O'Brien, F. J., Taylor, D. & Lee, T. C. The effect of bone microstructure on the initiation and growth of microcracks. *J. Orthop. Res.* **23**, 475–480 (2005).
56. Milovanovic, P. et al. Bone tissue aging affects mineralization of cement lines. *Bone* **110**, 187–193 (2018).
57. Skedros, J. G., Holmes, J. L., Vajda, E. G. & Bloebaum, R. D. Cement lines of secondary osteons in human bone are not mineral-deficient: New data in a historical perspective. *Anat. Rec. A Discov. Mol. Cell. Evol.* **286A**, 781–803 (2005).
58. Wittig, N. K. et al. Bone biomineral properties vary across human osteonal bone. *ACS Nano* **13**, 12949–12956 (2019).
59. Giannuzzi, L. A. & Stevie, F. A. *Introduction to Focused Ion Beams* (Springer, 2005).
60. Phaneuf, M. Applications of focused ion beam microscopy to materials science specimens. *Micron* **30**, 277–288 (1999).
61. Berger, C. et al. Cryo-electron tomography on focused ion beam lamellae transforms structural cell biology. *Nat. Methods* **20**, 499–511 (2023).
62. Grandfield, K. & Engqvist, H. Focused ion beam in the study of biomaterials and biological matter. *Adv. Mater. Sci. Eng.* **2012**, 1–6 (2012).
63. Echlin, M. P., Husseini, N. S., Nees, J. A. & Pollock, T. M. A new femtosecond laser-based tomography technique for multiphase materials. *Adv. Mater.* **23**, 2339–2342 (2011).
64. Echlin, M. P., Straw, M., Randolph, S., Filevich, J. & Pollock, T. M. The TriBeam system: Femtosecond laser ablation in situ SEM. *Mater. Charact.* **100**, 1–12 (2015).
65. Gemini, L. et al. Ablation of bone tissue by femtosecond laser: A path to high-resolution bone surgery. *Materials (Basel)* **14**, 2429 (2021).
66. Daskalova, A. & Husinsky, W. Ultra-short laser ablation of biological tissue. In *13th International School on Quantum Electronics: Laser Physics and Applications* (eds. Atanasov, P. A., Gateva, S. V., Avramov, L. A. & Serafetinides, A. A.) 473 (SPIE, 2005).
67. Gabel, C. V. Femtosecond lasers in biology: Nanoscale surgery with ultrafast optics. *Contemp. Phys.* **49**, 391–411 (2008).
68. Le Harzic, R. et al. Comparison of heat-affected zones due to nanosecond and femtosecond laser pulses using transmission electronic microscopy. *Appl. Phys. Lett.* **80**, 3886–3888 (2002).
69. Gholinia, A. et al. Exploration of fs-laser ablation parameter space for 2D/3D imaging of soft and hard materials by tri-beam microscopy. *Ultramicroscopy* **257**, 113903 (2024).
70. Paredes, A. M. MICROSCOPY | Transmission electron microscopy. In *Encyclopedia of Food Microbiology* 711–720 (Elsevier, 2014).
71. Deering, J. et al. Characterizing mineral ellipsoids in new bone formation at the interface of Ti6Al4V porous implants. *Adv. Mater. Interface* **10**, 2300333 (2023).
72. Shah, F. A., Thomsen, P. & Palmquist, A. A review of the impact of implant biomaterials on osteocytes. *J. Dent. Res.* **97**, 977–986 (2018).
73. Hasegawa, T. et al. Three-dimensional ultrastructure of osteocytes assessed by focused ion beam-scanning electron microscopy (FIB-SEM). *Histochem. Cell. Biol.* **149**, 423–432 (2018).
74. Buss, D. J., Rechav, K., Reznikov, N. & McKee, M. D. Mineral tessellation in mouse enthesis fibrocartilage, Achilles tendon, and Hyp calcifying enthesopathy: A shared 3D mineralization pattern. *Bone* **174**, 116818 (2023).
75. Peyrin, F., Dong, P., Pacureau, A. & Langer, M. Micro- and nano-CT for the study of bone ultrastructure. *Curr. Osteoporos. Rep.* **12**, 465–474 (2014).
76. Hesse, B. et al. Canalicular network morphology is the major determinant of the spatial distribution of mass density in human bone tissue: Evidence by means of synchrotron radiation phase-contrast nano-CT. *J. Bone Min. Res.* **30**, 346–356 (2015).

77. Yu, B., Pacureanu, A., Olivier, C., Cloetens, P. & Peyrin, F. Assessment of the human bone lacuno-canalicular network at the nanoscale and impact of spatial resolution. *Sci. Rep.* **10**, 4567 (2020).
78. Schneider, P., Meier, M., Wepf, R. & Müller, R. Towards quantitative 3D imaging of the osteocyte lacuno-canalicular network. *Bone* **47**, 848–858 (2010).
79. Suniaga, S. et al. Increased mechanical loading through controlled swimming exercise induces bone formation and mineralization in adult zebrafish. *Sci. Rep.* **8**, 3646 (2018).
80. Varga, P. et al. Synchrotron X-ray phase nano-tomography-based analysis of the lacunar–canalicular network morphology and its relation to the strains experienced by osteocytes in situ as predicted by case-specific finite element analysis. *Biomech. Model. Mechanobiol.* **14**, 267–282 (2015).
81. Wittig, N. K. et al. Canalicular junctions in the osteocyte lacuno-canalicular network of cortical bone. *ACS Nano* **13**, 6421–6430 (2019).
82. Schneider, P., Meier, M., Wepf, R. & Müller, R. Serial FIB/SEM imaging for quantitative 3D assessment of the osteocyte lacuno-canalicular network. *Bone* **49**, 304–311 (2011).

Acknowledgments

The authors are grateful to Cheryl Quenneville, Ph.D. (Department of Mechanical Engineering, McMaster University, Hamilton, Canada), for providing the human bone samples and to Kelly Lau, Aarani Subramaniam, Jia Wu, and Oksana Chunitska for sample embedding and polishing (all in the Department of Materials Science and Engineering at McMaster University). The authors also thank Jhoynner Martinez (Canadian Center for Electron Microscopy, McMaster University) for sample coating; and Mouhanad Babi, Ph.D. (McMaster Centre for Advanced Light Microscopy), for light microscopy imaging of sample overview.

Author contributions

T.T.: Conceptualization; data curation; formal analysis; funding acquisition; investigation; methodology; project administration; supervision; validation; visualization; writing – original draft; writing – review and editing. T.C.: Data curation; formal analysis; investigation; methodology; validation; writing – review and editing. P.M.: Data curation; formal analysis; investigation; methodology; validation; writing – review and editing. W.L.: Formal analysis; investigation; validation; writing – review and editing. B.L.: Formal analysis; investigation; methodology; validation; writing – review and editing. K.G.: Conceptualization; formal analysis; investigation; methodology; project administration; resources; validation; writing – review and editing.

Funding

This work was supported by grants to T.T. from the National Science and Engineering Research Council (NSERC DGEER-2023-00371, RGPIN-2023-05593, ALLRP-587309-23). T.C. and P.M. were supported by the Canadian Centre for Electron Microscopy (CCEM), a Canada Foundation for Innovation Major Science Initiatives funded facility (also supported by NSERC and other government agencies).

Declarations

Competing interests

The authors declare no competing interests.

Additional information

Supplementary Information The online version contains supplementary material available at <https://doi.org/10.1038/s41598-024-72739-8>.

Correspondence and requests for materials should be addressed to T.T.

Reprints and permissions information is available at www.nature.com/reprints.

Publisher's note Springer Nature remains neutral with regard to jurisdictional claims in published maps and institutional affiliations.

Open Access This article is licensed under a Creative Commons Attribution-NonCommercial-NoDerivatives 4.0 International License, which permits any non-commercial use, sharing, distribution and reproduction in any medium or format, as long as you give appropriate credit to the original author(s) and the source, provide a link to the Creative Commons licence, and indicate if you modified the licensed material. You do not have permission under this licence to share adapted material derived from this article or parts of it. The images or other third party material in this article are included in the article's Creative Commons licence, unless indicated otherwise in a credit line to the material. If material is not included in the article's Creative Commons licence and your intended use is not permitted by statutory regulation or exceeds the permitted use, you will need to obtain permission directly from the copyright holder. To view a copy of this licence, visit <http://creativecommons.org/licenses/by-nc-nd/4.0/>.

© The Author(s) 2024